

Static Modeling of Miniaturized Pneumatic Artificial Muscles, Kinematic Analysis and Experiments on an Endoscopic End-effector

K. P. Ashwin, Ashitava Ghosal*

Abstract

In this paper, we present the design, development, modelling and experimental validation of an endoscopic attachment that can be used to independently position an endoscopic catheter tip to a desired location. Three Miniaturized Pneumatic Artificial Muscles (MPAMs) are used in a flexible endoscopic attachment, each MPAM is of 1.2 mm diameter and 45 mm in length and placed approximately 120 degrees apart within a pair of concentric springs. Pressurizing one or more MPAMs allows the tip to be positioned in a workspace which is approximately a hemispherical section of radius 45 mm. We present a new and improved theoretical model for pressure-deformation relationship of a MPAM using static equations of a pressurized thick cylinder and constraints due to the braids. Comparison with existing models show that the proposed model performs better and the errors predicted by the model is less than 5% with experiments. A new forward kinematic model relating the position and orientation of the tip of the end-effector with changes in MPAM lengths is developed. Finally, we present experimental results conducted on a prototype endoscopic attachment and show that our model could predict the pose of the end-effector with a maximum error of 2 ± 1 mm.

*Corresponding author, Department of Mechanical Engineering, Indian Institute of Science, Bangalore, 560012 INDIA e-mail: (asitava@iisc.ac.in).

1 Introduction

Endoscope is a diagnostic instrument which is inserted into a patient's gastrointestinal (GI) tract from the mouth with the primary objective of real-time inspection. The device is a flexible tube of approximately 1.5 m length and about 12 mm in diameter. It contains a camera, lighting system as well as a nozzle for pumping air and water from its distal tip. Most of the modern endoscopes are also equipped with one or two channels through which a medical instrument (catheter) can be pushed from the holding end till its working end protrudes from the distal tip of the endoscope. Though all endoscopes have the provision to actuate the distal tip of the endoscope in vertical and horizontal directions, endoscopes in general do not have a provision to actuate the catheter independent of the camera. A few automated endoscopic platforms have the ability to actuate gripping tools for performing surgery [1], [2]. In these platforms, positioning is achieved using an end-effector which is essentially a cable driven continuum robot [3], [4]. Though it is possible to achieve precise control using cable actuation ([4], [5], [6]), tissue damages or perforation could occur, if the end-effector is not properly manipulated, since the device becomes a stiff structure in the actuation plane when deployed. Hence, there has been considerable focus in developing devices which are soft and flexible for endoscopic applications [7].

McKibben actuators are more suitable in such applications since the actuators are compliant/flexible even in its actuated state and are lighter in weight. A McKibben actuator consists of an inflatable bladder which is braided on the lateral outer surface using a helical mesh of flexible but inextensible fibers [8]. Air is pumped into the bladder from one end while the other end is sealed, allowing the bladder to inflate. However, the inextensible braid restricts the deformation of the bladder in such a way that when the braiding angle is less than 54.7° , the bladder contracts along its length [9]. Miniaturized versions of PAM (MPAM) would be ideal for medical robotics since: a) they have high load carrying capacity b) their stiffness can be controlled by the internal pressure c) they have low weight, and d) are less expensive to manufacture (see also [10–13]). Although in [14], it is shown that the compliance in the cable actuated robots can be monitored using load cells and hence controlled (they use it to measure hard tissue properties), we believe that the MPAMs are inherently more compliant and the compliance can be better controlled. The similarity of PAMs with biological muscles and an advancement in control strategies have made the actuators

popular in bio-inspired robotics and medical robotics (see [15–19]). It is also observed from the above references that accurate model to depict the physics of pneumatic muscles is an essential requirement for improved performance of control system [20].

One of the earliest attempts in modeling McKibben actuators was made by Schulte [9]. Many researchers improved upon this basic model by considering other physical effects such as friction, material properties, non-uniform shape of cylinder, thermal expansion effect as well as various energy losses [21–23]. A comparison between the pressure-deformation characteristics of MPAM used in this work with some of the easily implemented theoretical models such as in [9], [24] and [25] is shown in section 3.2 of this paper. It can be seen that even though many models can describe a standard PAM characteristics with reasonable accuracy, most of them deviate considerably when applied to an MPAM. In [10] and [12], the authors developed mathematical models for MPAM by modifying the existing PAM models. However, it is required to calculate extra parameters and correction factors by means of prior experimentation and curve fitting. A mathematical model which can accurately describe pressure-deformation relationship of MPAM and can handle changes in physical parameters of the actuator with reliable consistency is necessary for developing a robust kinematic model for the end-effector and for control.

Due to the small overall diameter and high power to weight ratio, multiple MPAMs could be combined to develop a continuum robot. In this paper, we introduce the design and analysis of such an end-effector, which can deflect an endoscopic catheter independent of camera. Firstly, we develop a new and improved pressure-deformation model of an MPAM that can predict the contraction in an MPAM consistent with parameter changes. A forward kinematics model of the end-effector with inputs from MPAM statics is developed and then experimentally validated. In Section 2, the geometry and design of the end-effector as well as the MPAMs used in the end-effector are introduced. Characterization of MPAMs used to actuate the end-effector is detailed in Section 3. An improved model for MPAM is developed and validated in this section. In section 4, the forward kinematics of end-effector is presented. Numerical simulation results and experimental results are compared in section 5 and it is shown that there is good agreement between both sets of results. Conclusions are presented in section 6.

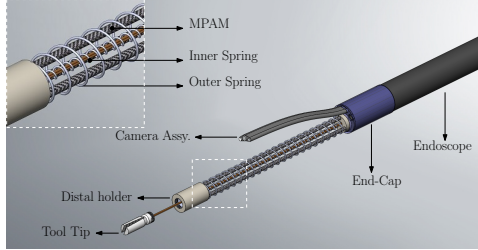


Figure 1: End-effector and camera assembly deployed from endoscope

2 Design of End-effector

The proposed modification at the distal end of endoscope is shown in Fig. 1. The system consists of three main components: a) A camera assembly which holds camera, lighting system and a nozzle for spraying water as well as pump air, b) An end-effector assembly with endoscopic tool/catheter attached to the tip which can be deflected independent of the camera assembly, and c) A spring loaded end-cap which can be retracted using cables to reveal the end-effector assembly as well as the camera assembly. The conceptual design of the proposed modification in endoscopic tip is similar to that of [4]. Instead of parallel mechanism used in deploying the sub-assemblies, the camera subsystem is assembled in an initially pre-deformed form as shown in the figure (deployed state). The end-cap will be spring loaded so that in its neutral state, both the end-effector assembly as well as the visual assembly will be concealed. By pulling the end-cap backwards, both the assemblies will be revealed which constitute the deployment of the system. In order for the camera(visual) assembly to be resting overhead, the whole camera subsystem is assembled in a pre-deformed form as shown in the figure (deployed state). Hence, the subsystem when concealed by end-cap will be stressed and in the deployed state, will be stress free. This way, the design is very much simplified. Another major difference here is the use of MPAM in actuation.

In this paper, we focus exclusively on the end-effector assembly which is similar to the design proposed in a previous work [26]. The design consists of two concentric helical springs with three MPAMs positioned parallel to the axis of the springs in the space between the inner and outer springs. The three MPAMs are approximately 120 degrees apart and are capped at the ends along with the springs using holders¹. The MPAMs can be energized

¹Although, not shown in the prototype, the outer springs can be covered with a flexible



Figure 2: End-effector prototype and fabricated MPAM

using pressurized air applied through tubes connected to a reservoir. The catheter/instrument is fixed at the tip of end-effector and the inner spring acts as a conduit for cables used to actuate the same. Both the springs have low axial as well as transverse stiffness with the axial stiffness of inner spring slightly higher compared to the outer spring. This enables the the tip of inner spring to act as a fulcrum whenever the MPAM contracts, facilitating its deflection. The maximum length of end-effector is restricted to about 50 mm considering the depth of vision of camera of the endoscope and size of the operating region in the GI tract. Since the end-effector needs to be housed alongside other accessories at the tip of the endoscope, the outer diameter of end-effector needs to be less than about 8 mm. Due to the arrangement and contraction in the MPAMs, by actuating two MPAMs at a time, the tip of end-effector can be positioned in a section of a hemisphere. Fig. 2 shows a prototype of the developed end-effector assembly as well as the in-house fabricated MPAM. The end-effector is 55 mm long (including holders) and has 9 mm outer diameter. The MPAM used in the end-effector is 45 mm long with 1.2 mm outer diameter. By pressurizing or more MPAMs, the tip of the end-effector can trace an approximate hemispherical section of radius 45 mm.

The layout of pneumatic circuit used to actuate MPAM is shown in Fig. 3. A pneumatic compressor of maximum output pressure 1034 kPa (150 psi) is connected to a 1 liter air reservoir which is used to deliver high pressure air to the MPAM. A pressure regulating circuit operates the compressor when the value of pressure in reservoir falls below certain threshold thereby maintaining a plastic layer so that it will not be exposed to GI tract fluids.

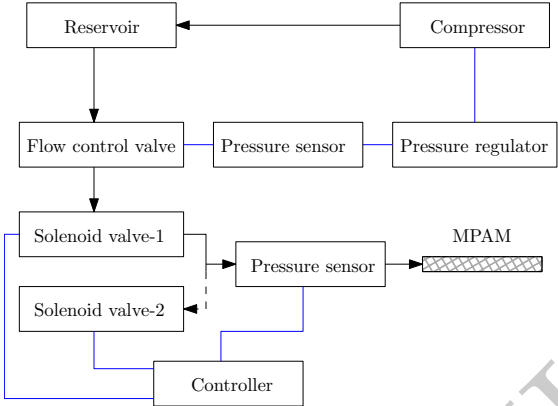


Figure 3: Layout of pneumatic circuit

taining availability of 827 kPa (120 psi) pressure at all times. The volume of air in the MPAM is approximately 30 mm^3 and even in case of rupture, this small volume is not expected to result in safety issue. In addition, the flow control valve limits the volume flow rate of air into the MPAM to avoid sudden bleeding of compressed air from the reservoir to the MPAM. Two proportional valves are used to control pressure inside air muscle – one for pressurizing the MPAM and the other for bleeding. A Honeywell pressure transducer (with range of 0 to 1034 kPa) is connected in series with MPAM to measure the inner pressure. An ATmel ATMega2560 micro-controller board interfaced with MATLAB [27] controls the proportional valves through a current driver circuit to maintain desired value of pressure inside the MPAM. For characterization of MPAM, deformation of single MPAM is captured using high resolution camera and the changes in length are obtained using image processing. In order to keep a straight alignment of the MPAM during the experiments, a 5 gram weight ($\sim 0.05 \text{ N}$) is applied on the free end of MPAM which is vertically hung. The maximum possible error due to measurement is about 0.2 mm which is due to identifying accurate pixel points in camera image. The experimental plots are shown with error bars obtained from at least 5 sets of experiments.

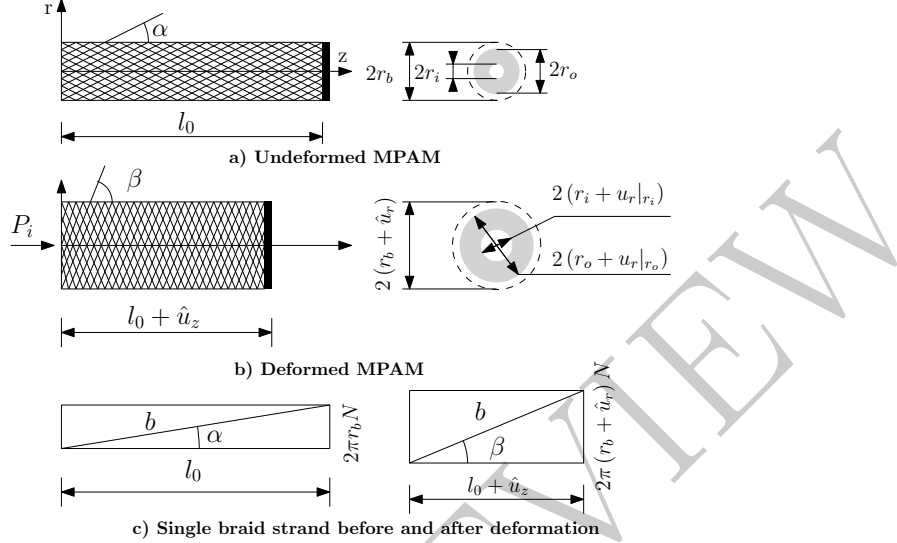


Figure 4: MPAM nomenclature

3 Characterization of MPAM

Fig. 4 shows the schematic of MPAM with the nomenclature used in modeling the MPAM in this work. The symbols r_o , r_i and l_o denote the outer radius, inner radius and length of inner silicone tube, respectively. The symbols α and β denote the angle of winding of MPAM before and after deformation, \hat{u}_z and \hat{u}_r represent axial and radial displacements of braided sleeve while u_z and u_r represent axial and radial displacements of silicone tube. The constant b represents the length of a single braid strand, N denotes the number of windings of braid and P_i is the input pressure. Since the end-effector is assumed to be operating in slow speeds, only static analysis is considered in this paper.

3.1 Proposed Model for MPAM

The inflation problem of silicone tube can be described as the solution to the linearized elastic equilibrium equations of a thick cylinder under pressure [28]:

$$\frac{\partial}{\partial r} \left(\frac{1}{r} \frac{\partial (r u_r)}{\partial r} \right) = 0, \quad \frac{\partial^2 u_z}{\partial z^2} = 0$$

which have an analytical solution of the form

$$u_r = c_1 r + \frac{c_2}{r}, \quad u_z = c_3 z + c_4 \quad (1)$$

where c_i , $i = 1, 2, 3, 4$ are the constants of integration. The boundary conditions on radial and axial stresses τ_{rr} and τ_{zz} , as well as the end displacements are

$$\tau_{rr}|_{r=r_i} = -P_i, \quad \tau_{rr}|_{r=r_o} = -P_o, \quad \tau_{zz}|_{z=l_0} = P_s \quad (2)$$

$$u_z(r, l = 0) = 0, \quad u_r(r, l = 0) = u_r(r, l = l_0) = 0 \quad (3)$$

where P_o , P_s are the radial pressure on the outer surface and pressure on the axial end, respectively.

Applying the boundary conditions and solving for the constants, we get

$$\begin{aligned} c_1 &= \frac{(\lambda + 2\mu)}{2\mu(3\lambda + 2\mu)} \left[\frac{P_i r_i^2}{r_o^2 - r_i^2} + \frac{P_o r_o^2}{r_o^2 - r_i^2} - \frac{P_s \lambda}{\lambda + 2\mu} \right] \\ c_2 &= \frac{1}{2\mu} \left[\frac{r_i^2 r_o^2}{r_o^2 - r_i^2} \right] (P_i - P_o) \\ c_3 &= \frac{\lambda}{\mu(3\lambda + 2\mu)} \left[-\frac{P_i r_i^2}{r_o^2 - r_i^2} + \frac{P_o r_o^2}{r_o^2 - r_i^2} + P_s \frac{\lambda + \mu}{\lambda} \right] \\ c_4 &= 0 \end{aligned} \quad (4)$$

where λ and μ are Lame's parameters. Since the braid fibers are assumed to be inextensible, they act as a constraint to the above displacements.

From (1), we see that the cylindrical tube remains cylindrical even after deformation. Hence, referring to Fig. 4, we can relate the initial and final configurations of a single braid strand as previously derived in [29]

$$l_0 = b \cos \alpha, \quad 2\pi r_b N = b \sin \alpha \quad (5)$$

$$l_0 + \hat{u}_z = b \cos \beta, \quad 2\pi(r_b + \hat{u}_r) N = b \sin \beta \quad (6)$$

When MPAM is pressurized, the axial force F_e acting at the free end is unevenly distributed among the braided sleeve and silicone tube as F_{nyl} and F_{sil} respectively (refer Fig. 5). In order to determine the values of these forces, we consider the deformation at the free end of MPAM. The deformation at the tip of the MPAM, denoted by Δ is same as the deformation of the nylon braid Δ_{nyl} and the deformation of the silicone tube Δ_{sil} . From Fig. 5,

$$\Delta_{nyl} = \frac{\hat{F}b}{\hat{A}_{nyl} E_{nyl}} \cos \alpha \quad (7)$$

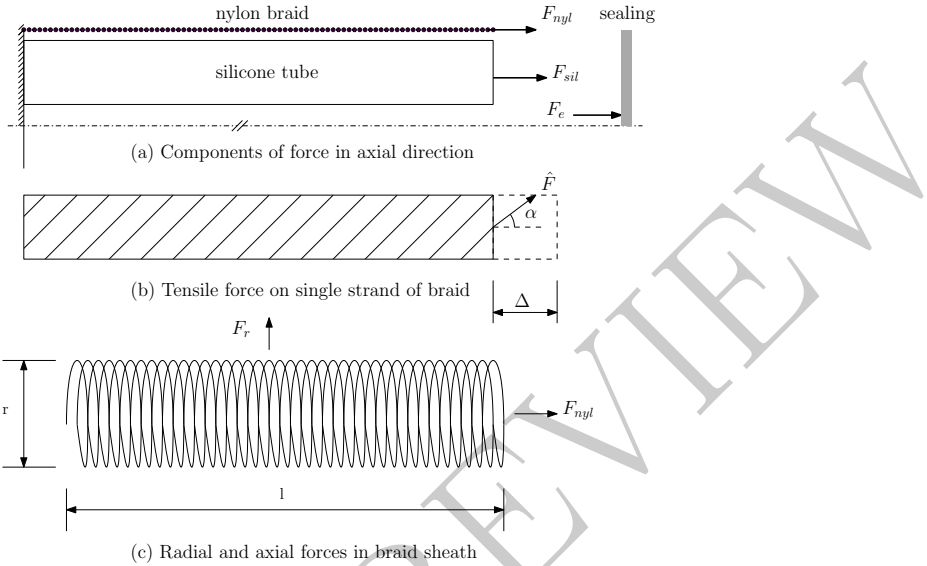


Figure 5: Braid statics

where $\hat{F} = \frac{F_{nyl}}{m} \cos \alpha$ is the force acting on a single strand of braid – m is the number of braid strands in the sleeve, \hat{A}_{nyl} is the area of cross section of single nylon strand and E_{nyl} is the modulus of elasticity of nylon. Substituting the values, we get

$$\Delta_{nyl} = \frac{F_{nyl}l_0 \cos \alpha}{m\hat{A}_{nyl}E_{nyl}} \quad (8)$$

where we have used the first expression in (5). For the silicone tube, deflection at the tip is calculated using (1) and (4) with $P_i = P_o = 0$, and we have

$$\Delta_{sil} = \frac{(\lambda + \mu)}{\mu(3\lambda + 2\mu)} P_s l_0 = \frac{F_{sil}l_0}{A_{sil}E_{sil}} \quad (9)$$

where the Poisson's ratio ν is assumed to be approximately equal to 0.5 and A_{sil} and E_{sil} are cross sectional area and modulus of elasticity of silicone tube, respectively. Since $F_e = F_{nyl} + F_{sil}$, equating (8) and (9) and re-arranging, we get

$$F_{nyl} = \frac{F_e m \hat{A}_{nyl} E_{nyl}}{m \hat{A}_{nyl} E_{nyl} + \cos \alpha A_{sil} E_{sil}} \quad (10)$$

and

$$F_{\text{sil}} = \frac{F_e \cos \alpha A_{\text{sil}} E_{\text{sil}}}{m \hat{A}_{\text{nyl}} E_{\text{nyl}} + \cos \alpha A_{\text{sil}} E_{\text{sil}}} \quad (11)$$

The helical arrangement of the braid converts axial force on nylon sleeve F_{nyl} to radial force F_r as shown in Fig. 5(c). To relate the forces on braid in axial as well as radial directions, we use the principle of virtual work,

$$F_r \delta r + F_{\text{nyl}} \delta l = 0 \quad (12)$$

where δr and δl are the virtual displacements in radial and axial directions, respectively. From (5) and (6), we get

$$\delta l = -b \sin \beta \delta \beta, \quad \delta r = b \frac{r_b \cos \beta}{l_0 \tan \alpha} \delta \beta \quad (13)$$

where $l = l_0 + \hat{u}_z$, $r = r_b + \hat{u}_r$ are the length and radius of sleeve at angle β . Substituting in (12) and rearranging, we get

$$F_r = F_{\text{nyl}} \frac{l_0}{r_b} \tan \beta \tan \alpha \quad (14)$$

The equation (14) represents the radial force required on braid sleeve for a given value of axial force in order to maintain equilibrium when the braid is at deformed angle β .

The equations (1) and (4) with expressions for F_e and F_r can be combined to form the mathematical model for MPAM. However, as shown in the experimental results in Fig. 6, the displacement versus pressure curve of MPAM is divided into two phases and separate governing equations are required for the two phases. It is noticed that for a small value of pressure (< 140 kPa), the air muscle elongates by a very small amount before the contraction starts. This is due to the gap δ (of the order of 0.04 mm) between the tube and nylon sleeve during fabrication. Hence, upon inflation of MPAM, the initial stage will be the expansion of silicone tube till the outer surface of silicone tube makes contact with the nylon sleeve. The deformation during the first phase is hence calculated using (1) and (4) without any constraints, till outer radius of silicone tube and the radius of braided sleeve are equal. The value of pressure \bar{P}_i at this contact point can be calculated by equating the outer radius of silicone tube and radius of braid as follows:

At the contact point,

$$r_o + u_r|_{r_o} = r_b + \hat{u}_r = r_o + \delta + \hat{u}_r \quad (15)$$

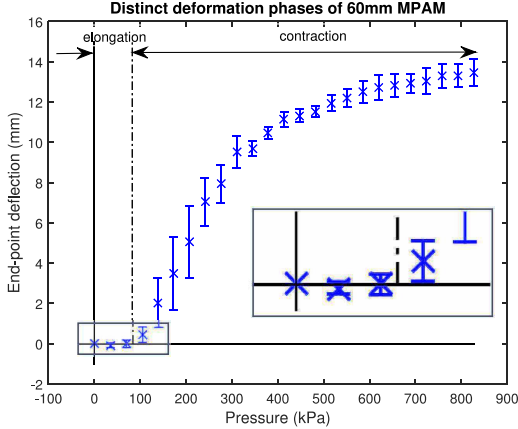


Figure 6: Deformation phases of MPAM (inset – elongation part zoomed)

Also, $P_o = 0$ and $P_s = P_i \frac{r_i^2}{r_o^2 - r_i^2} + P_{sil}$ in this phase, where P_{sil} is the pressure applied on silicone tube due to external axial load. From (5) and (6), we get

$$\cos^2 \alpha \left(1 + \frac{\hat{u}_z}{l_0}\right)^2 + \sin^2 \alpha \left(1 + \frac{\hat{u}_r}{r_b}\right)^2 = 1 \quad (16)$$

which relates the radial and axial displacements of braid sleeve. Since the braid is attached to silicone tube at either ends, $u_z|_{l_0} = \hat{u}_z$ at all times. Substituting $\hat{u}_z = u_z|_{l_0} = c_3 l_0$ in the above equation, the radial displacement of braid is given as

$$\hat{u}_r = r_b \left\{ \frac{1}{\sin \alpha} \sqrt{1 - \cos^2 \alpha (1 + c_3)^2} - 1 \right\} \quad (17)$$

From (15) and (1), we get

$$c_1 r_o + \frac{c_2}{r_o} = \delta + r_b \left\{ \frac{1}{\sin \alpha} \sqrt{1 - \cos^2 \alpha (1 + c_3)^2} - 1 \right\} \quad (18)$$

The above equation is a function of applied pressure P_i and is solved numerically to get the inflection pressure \bar{P}_i above which MPAM will start the contraction phase.

In the second phase, the braid makes contact with the tube and is assumed to move over the tube surface without slipping. The total external force F_e

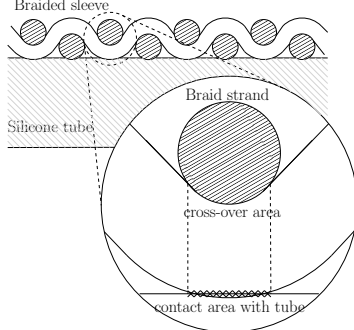


Figure 7: Area of contact between silicone tube and braided sleeve

acting on the axial end of MPAM is due to three components,

$$F_e = F + F_{P_i} + F_u \quad (19)$$

where F is the applied axial load, $F_{P_i} = P_i(\pi r_i^2)$ is the force at the axial end produced by the input pressure acting on side walls and F_u are the unaccounted forces such as friction between braid sleeves as well as friction between the sleeve and the tube and other unmodelled non-linear effects. These three axial forces are divided among the sleeve and tube as given in (10) and (11). The axial force on the sleeve F_{nyl} is then converted to radial force on the tube using (14). Pressure acting on the tube surface due to this radial force is given by $P_b = \frac{F_r}{A_b}$ where A_b is the surface area of contact of braided mesh with the silicone tube. The value of A_b is difficult to measure experimentally and estimate analytically [22,30] because of the small surface area. We assume that the contact area of braid on surface of tube is same as the contact area between the braid strands at braid cross-over points when the applied axial force is zero (refer Fig. 7). The expression for this contact area in terms of deformed braid angle is derived in [30] and is given as

$$A_{\text{contact}} = \frac{b^2 \sin^2 \alpha_{\min} \cos^2 \alpha_{\min}}{N \sin \beta \cos \beta} = \frac{\sin^2 \alpha_{\min} \cos^2 \alpha_{\min}}{\sin^2 \beta \cos^2 \beta} A_{\text{cyl}} \quad (20)$$

where $\alpha_{\min} = \frac{1}{2} \sin^{-1} \left(\frac{2mNr_n}{b} \right)$ is the angle when the braided sleeve is fully stretched (least possible angle for a given braid pattern), r_n is half the diameter of single braid strand and A_{cyl} is the lateral surface area of cylinder after deformation.

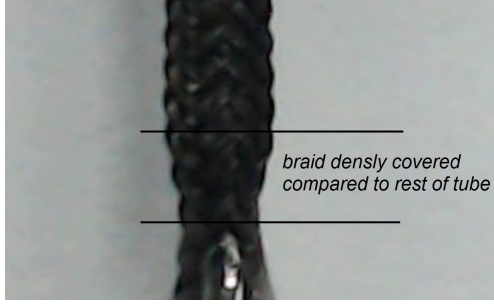


Figure 8: End-effect due to braiding

It is observed from experiments, that the contact area at a length of ϕ ($\sim 5\text{mm}$) from each axial ends is much higher compared to the middle of tube (refer Fig. 8). This is because at the ends, deformation is not cylindrical but tapered unlike the assumption in the formulation. This effect is to be included in the formulation since it accounts for approximately 25 % for a 40 mm MPAM. Contribution of end-tapering in theoretical models is studied by a few researchers (see [21] and [31]). The simplest model considers the taper as a conical frustum. In the case of MPAM used in this paper, the tapered end is densely braided unlike the rest of the cylindrical surface. Hence, we assume full contact between silicone tube and braid at these tapered ends.

Combining the two we get the total area of contact as

$$A_b = \frac{\sin^2 \alpha_{\min} \cos^2 \alpha_{\min}}{\sin^2 \beta \cos^2 \beta} A^{\text{cyl}} + 2A^{\text{conical}} \quad (21)$$

where $A^{\text{conical}} = \pi (r_b + r) (\phi + c_3 \phi)$ is the surface area of contact at conical ends and $A^{\text{cyl}} = 2\pi r ((l_0 - 2\phi) + c_3 (l_0 - 2\phi))$ is the area of lateral cylindrical surface.

In order to simplify the calculations in second phase, we consider the second phase as a problem of deformation with the dimensions of tube and sleeve modified as per the values at the inflection point:

$$r_o \rightarrow r_o + u_r|_{r_o}, \quad r_i \rightarrow r_i + u_r|_{r_i}, \quad l_o \rightarrow l_o + u_z|_{l_o}$$

For the new arrangement to be in equilibrium, all the traction forces on surfaces must be zero. Hence, we also modify the input pressure to $P_i \rightarrow P_i - \bar{P}_i$, pressure at the axial end to $P_s \rightarrow P_s - \bar{P}_s$ and the radial outer surface pressure on silicone tube (equal to the pressure applied by braid) to

$P_o = P_b \rightarrow P_b - \bar{P}_b$. It may be mentioned that (\cdot) denote the corresponding values of pressures at the inflection point.

In this second phase, we also have the constraints on displacements $u_r|_{r_b} = \hat{u}_r$ and $u_z|_{l_o} = \hat{u}_z$. The displacements as obtained from (5) and (6), can be written as

$$\hat{u}_z = l_0 \left(\frac{\cos \beta}{\cos \alpha} - 1 \right), \quad \hat{u}_r = r_b \left(\frac{\sin \beta}{\sin \alpha} - 1 \right) \quad (22)$$

Since displacement of sleeve and tube are same in the second phase, the constants c_i will be (from (22)),

$$c_1 + \frac{c_2}{r_o^2} = \left(\frac{\sin \beta}{\sin \alpha} - 1 \right), \quad c_3 = \left(\frac{\cos \beta}{\cos \alpha} - 1 \right) \quad (23)$$

The solution procedure for the second phase can now be summarized as follows: The value of pressure on the outer surface of tube, $P_b = \frac{F_r}{A_b}$ can be obtained using (14), (10) and (19) for F_r and (21) for A_b . Given all parameter values, there will be two unknown quantities F_u and β in the expression for P_b . Then the six equations in (4) and (23) are solved for 6 unknowns, namely c_1, c_2, c_3, c_4, F_u and β . The values of c_i are in turn plugged into (1) to calculate the final deformation of MPAM. One major advantage of the above formulation compared to the existing models in the literature is that all unaccounted forces which are required to maintain static equilibrium of MPAM such as frictional force and thermal expansion effects are included in the term F_u which is obtained from the solution of the six equations. To study the dependency of F_u on the individual factors, one needs to break the axial force F_u into its components as has been done for static frictional force and force due to conical end-effects [21]. However, we believe that this compartmentalization of forces will not still be accurate since the models for these factors are not accurately known and one might miss out on other contributing factors. A study on the factors affecting F_u is beyond the scope of this paper.

3.2 Validation of Proposed Model for MPAM

In order to validate the above developed theoretical model, deflection values are calculated numerically using ‘*fsolve*’ routine in MATLAB and plotted alongside measured values for a pressure range from 0 to 827 kPa (120 psi).

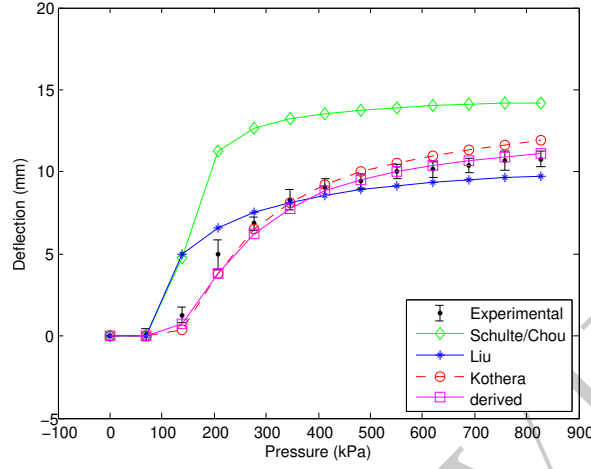


Figure 9: Experimental validation for 40 mm MPAM $\alpha = 36^\circ$, $r_i = 0.25$ mm, $r_o = 0.55$ mm, $r_n = 0.04$ mm, $m = 30$, $\phi = 5$ mm, $E = 0.35$ MPa, $\nu = 0.499$.

Three models by Schulte [9], Liu-Rahn [24] as well as Kothera et.al. [25] are also plotted for comparison. As mentioned in Section 1, most of the theoretical models available in the literature for PAMs require accurate determination of physical parameters such as friction coefficient, thermal expansion coefficient or nonlinear material properties to calculate end-point deformation. This requires sophisticated measurement techniques due to the miniature size of fabricated muscle. Due to this reason, we chose for comparison, only those models which have parameters that can be easily measured as well as implemented. Fig. 9 shows the plot for deflection of 40 mm long MPAM where it can be seen that theoretical results match experimental values very well. The computation time for the serially coded routine was approximately 0.04 seconds on an Intel Pentium PC at 2.0 GHz.

To check the consistency of the model for an MPAM with different initial length, the results obtained with length 60 mm while keeping all the other parameters same, is shown in Fig. 10. For both the lengths, the deformation curve is well within the error bounds of measured values. The RMS errors calculated from mean values are 4.6% and 2% of maximum contraction for 40 mm and 60 mm MPAM respectively. Simulation results for MPAM with slightly higher braiding angle is shown in Fig. 11. The gap between silicone tube as well as the braid was higher in this case for the selected specimen ($\delta = 0.06$ mm). The applied force vs axial displacement for a 45 mm MPAM

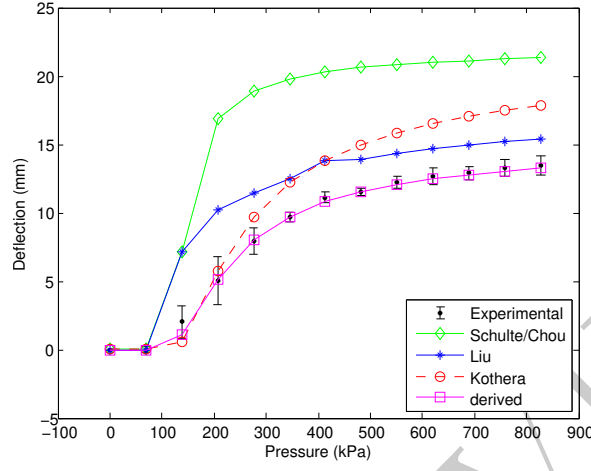


Figure 10: Experimental validation for 60 mm MPAM. $\alpha = 36^\circ$, $r_i = 0.25$ mm, $r_o = 0.55$ mm, $r_n = 0.04$ mm, $m = 30$, $\phi = 5$ mm, $E = 0.35$ MPa, $\nu = 0.499$.

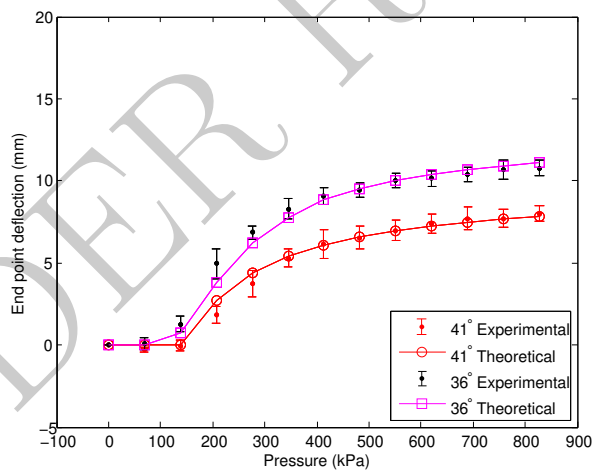


Figure 11: Experimental validation for different angle of windings $l_o = 40$ mm, $r_i = 0.25$ mm, $r_o = 0.55$ mm, $r_n = 0.04$ mm, $m = 30$, $\phi = 5$ mm, $E = 0.35$ MPa, $\nu = 0.499$.

from fully contracted position at 758 kPa (110 psi) is plotted in Fig. 12. The larger error at higher applied force is due to the fact that at higher

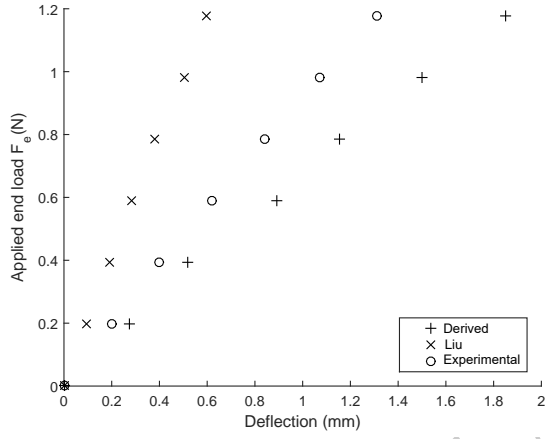


Figure 12: Axial force vs displacement comparison $P_i = 758$ kPa, $\alpha = 36^\circ$, $l_o = 45$ mm, $r_i = 0.25$ mm, $r_o = 0.55$ mm, $r_n = 0.04$ mm, $m = 30$, $\phi = 5$ mm, $E = 0.35$ MPa, $\nu = 0.499$

forces, the surface area of contact between braid and tube is higher and the formulation will have to include protrusion effects as well as other complex contact modeling. However, the trend in curve is consistent with the actual values and there is a maximum error of 0.6 mm at the highest value of applied force. In terms of the final deformation (including the free deformation), this value corresponds to less than 2% error from the measured value.

4 Kinematics of end-effector

The developed end-effector shown in Fig. 2 is similar to the tendon driven robots based on the actuation technique. The inner spring acts as the backbone and the tendons are replaced by MPAMs. The kinematic analysis of such designs is available in the literature (see, for example, [3,32–34]). However, unlike in the conventional tendon driven robots, there are no guiding discs in our prototype. The presence of guiding discs limits the radial expansion and also generates friction thereby reducing the overall contraction. In the absence of guiding discs, the MPAMs can drift sideways once the end-effector is deflected as shown in Fig. 13, and as a consequence existing kinematic models for continuum robots cannot be used for the end-effector developed in this work.

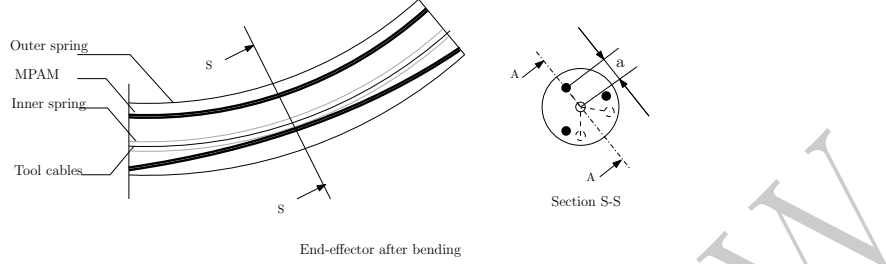


Figure 13: Tendon driven robot analogy – dotted and filled circles are initial and final position

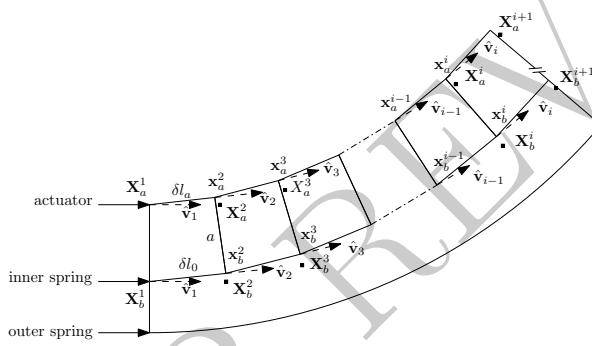


Figure 14: Backbone-actuator profile

To take into account the absence of guiding disks, we developed a new kinematic model which relates the position of the tip of the end-effector as a function of the deformation in the three MPAMs. The main assumption is that when the end-effector is deflected, the 3 MPAMs move minimum distance so as to achieve an equilibrium position. Fig. 14 shows the backbone-actuator assembly along an axial section of end-effector (section AA from Fig. 13). The entire length of end-effector is discretized into n segments, each segment representing the length at which the outer spring comes in contact with the MPAM. An axial force will cause change in length in inner spring. However, since we are only considering transverse loading on the end-effector due to the moment applied by the MPAM, the spring (backbone) is assumed to be of constant length throughout the actuation. The length of a backbone in a segment is given as $\delta l_0 = l_0/n$ and the length of actuator in a segment is $\delta l_a = l_a/n$ where l_a is the final length of MPAM after

pressurizing. In un-actuated state, the segment forms a quadrilateral with co-ordinates $\mathbf{X}_b^i, \mathbf{X}_b^{i+1}, \mathbf{X}_a^{i+1}, \mathbf{X}_a^i$ as shown in the figure where the subscripts b and a represent backbone and MPAM, respectively and $i = 1$ for segment at the base of end-effector and $i = n$ at the tip. The natural undeformed initial positions \mathbf{X}_b^{i+1} and \mathbf{X}_a^{i+1} are found out as

$$\mathbf{X}_b^{i+1} = \mathbf{X}_b^i + \delta l_0 \hat{\mathbf{v}}_i \quad \text{and} \quad \mathbf{X}_a^{i+1} = \mathbf{X}_a^i + \delta l_a \hat{\mathbf{v}}_i \quad (24)$$

$$\text{where, } \hat{\mathbf{v}}_i = \frac{\mathbf{X}_b^i - \mathbf{X}_b^{i-1}}{\|\mathbf{X}_b^i - \mathbf{X}_b^{i-1}\|} \quad (25)$$

For the initial segment $i = 1$, the unit vector $\hat{\mathbf{v}}_1$ is perpendicular to the vector $\mathbf{X}_b^1 - \mathbf{X}_a^1$ along the initial axis of end-effector.

After deformation, the quadrilateral changes to $\mathbf{X}_b^i, \mathbf{x}_b^{i+1}, \mathbf{x}_a^{i+1}, \mathbf{X}_a^i$ where vectors in lower case characters represent deformed position. Since the distance between backbone and MPAMs are constrained by the outer spring to a fixed value, the length $\|\mathbf{x}_b^{i+1} - \mathbf{x}_a^{i+1}\| = a$ at all times. The deformed quadrilateral could be positioned in different configurations depending on the angle formed by $\mathbf{x}_a^{i+1} - \mathbf{X}_a^i$ and $\mathbf{X}_b^i - \mathbf{X}_a^i$. Here, the natural configuration is assumed to be the one which minimizes the displacement of tip \mathbf{x}_a^{i+1} [35]. To find the deformed configuration, we formulate an optimization problem

$$\begin{aligned} & \min_{\mathbf{x}_b^{i+1}, \mathbf{x}_a^{i+1}} \|\mathbf{X}_a^i - \mathbf{x}_a^{i+1}\| \\ & \text{Subject to : } \|\mathbf{x}_b^{i+1} - \mathbf{X}_b^i\| = \delta l_0, \\ & \|\mathbf{x}_a^{i+1} - \mathbf{X}_a^i\| = \delta l_a, \quad \|\mathbf{x}_b^{i+1} - \mathbf{x}_a^{i+1}\| = a \end{aligned} \quad (26)$$

The solution to the above optimization problem gives the co-ordinates of tips \mathbf{x}_b^{i+1} and \mathbf{x}_a^{i+1} . The iterative method starts from the base segment and proceeds towards the tip of the end-effector to determine the final pose of the end-effector backbone and the actuated MPAM.

In the case of two MPAMs actuated together, the resultant moment due to these actuators can be written as

$$\mathbf{M} = \mathbf{a}_i \times \mathbf{F}_i + \mathbf{a}_j \times \mathbf{F}_j = \mathbf{a}_r \times \mathbf{F}_{\text{res}} \quad (27)$$

where $\mathbf{a}_{i,j}$ are the position vectors of the tip of i^{th} and j^{th} MPAM and $\mathbf{F}_{i,j}$ are the applied forces on end-effector by the MPAMs, \mathbf{a}_r is the position vector

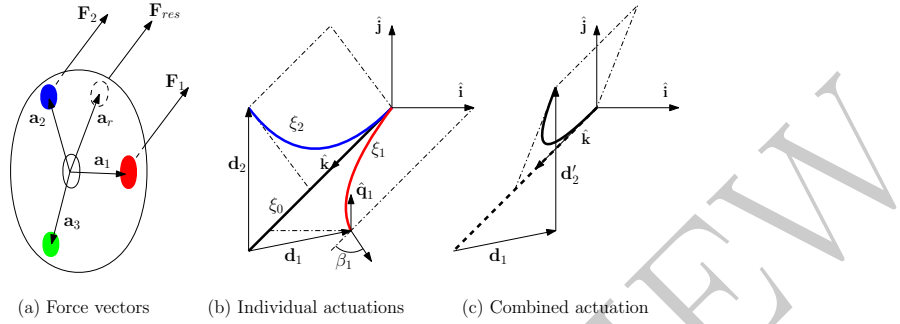


Figure 15: Displacement vector addition

of a hypothetical actuator whose resultant force $F_{res} = F_1 + F_2$ will provide the same moment as due to the other two MPAMs actuated together (see Fig. 15(a)). From basic mechanics, the direction of the hypothetical actuator is given by

$$l_r = \frac{(l_1 F_1 + l_2 F_2)}{F_1 + F_2}, \quad m_r = \frac{(m_1 F_1 + m_2 F_2)}{F_1 + F_2} \quad (28)$$

where $l_i, m_i, i = 1, 2$ determine the directions of \mathbf{F}_1 and \mathbf{F}_2 and l_r, m_r also determine the plane of bending of the end-effector.

If two MPAMs are pressurized simultaneously, the axial force generated at the tip will be large enough to compress the inner spring. Hence, MPAMs are pressurized only one after the other. From Fig. 15(b), the tip deflection from initial position (ξ_0 in the figure) due to individual actuation of two MPAMs (given by curves ξ_1 and ξ_2) are along the direction of force vectors represented by \mathbf{d}_1 and \mathbf{d}_2 respectively. When these MPAMs are pressurized successively, with \mathbf{d}_1 followed by \mathbf{d}_2 , then the vector \mathbf{d}_2 is rotated about β_1 angle which is the angle at the tip of ξ_1 with respect to \hat{k} axis. The rotation will be along the axis of rotation of the end-effector when only the first MPAM is actuated (unit vector $\hat{\mathbf{q}}_1$ shown in Fig. 15). The resultant deflection will be in the direction of vector sum of \mathbf{d}_1 and \mathbf{d}'_2 where $\mathbf{d}'_2 = \hat{\mathbf{R}}(\hat{\mathbf{q}}_1, \beta_1)\mathbf{d}_2$ is the rotated vector (see Fig. 15(c)).

From the static model of MPAM derived in section 3.1, we obtain the deformed length corresponding to a given applied pressure and axial load. From the forward kinematic equations derived in section 4, we get the pose of end-effector corresponding to given displacement of MPAMs/tendons. Combining both the models, we obtain the pose of end-effector corresponding to

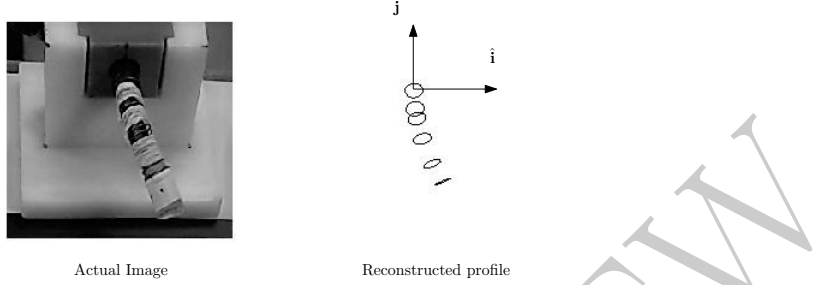


Figure 16: Profile reconstruction using image analysis

pressure applied at MPAMs.

5 Experimental validation

In order to validate the developed model, end-effector prototype is subjected to different values of pressure and the pose of end-effector after deflection is compared with the values obtained from theoretical model. Two cameras are used to capture images from different angles and the 3D co-ordinates of the central (backbone) curve of end-effector is obtained using multiple view image reconstruction techniques [36]. A thin flexible film of white colour is applied on the end effector surface to facilitate control point identification. A high contrast marking relative to the colour of end holder is made at the tip so that the marker is easily identified in the captured images. To find the co-ordinates of tip, respective pixels in the two images corresponding to the marker position is manually selected. The possible error in this method is in incorrectly identifying the marker pixels which will not be more than 4 pixels size for both the images. For the scale and measurement set up used, the maximum error in reconstruction is approximately 2 mm at the tip.

Fig. 16 shows the deformation of end-effector as well as the re-constructed profile when one MPAM is pressurized. It may be noted that the reconstructed profile is limited to the tip of MPAM which is at 45 mm from the base, while the end-effector tip extends up to 55 mm due to the distal holder. By actuating three MPAMs individually, it is found out that the MPAMs are positioned at 307.5° , 219° and 75° angles from the positive \hat{i} axis shown in Fig. 16. They are named R , G and B respectively for identification. By

applying a 0.1 N transverse load at the tip of the end-effector, a deflection of approximately 15 mm is obtained. The flexural rigidity is then calculated using the standard beam equation.

The solution to kinematics of end-effector considering the MPAM statics is carried out using an iterative scheme. At first, the deformation of a single MPAM for zero applied axial force is found out using the theoretical model discussed in section 3.1. This value of deformation is used to calculate δl_a and the optimization problem in (26) is solved to get the pose of end-effector. The displacement of tip δ_e from the original position is calculated from the theoretical pose of end-effector. The moment that may be applied at the tip of end-effector in order to produce the same deflection is calculated using the cantilever equation $\delta_e = ML^2/3EI$, where EI is the flexural rigidity of the end effector. Since moment $M = a \times F$, we get the axial force F that should be produced by the MPAM in order to get the same deflection. Using this value of F , the deformation of single MPAM is re-calculated and the same procedure is repeated till the change in final deflection of end-effector is within a specified tolerance.

In order to validate the theoretical model, a pressure of 689.4 kPa(100 psi) is applied to MPAM-*R* (refer Fig. 16). For no applied axial force, *R* gives $\Delta = 7.6$ mm contraction as per the derived theoretical model. The final length of MPAM will be $l_a = l_o - \Delta = 37.4$ mm. This value is used to predict the pose of end-effector using the kinematic model where 15 segments are used for computation (length of one segment is equal to the pitch of the outer spring). The final pose of end-effector gives a tip deflection of $\delta_e = 22.8$ mm. The force F which MPAM has to apply on end-effector so as to obtain this value of deflection is calculated to be $F^* = 1.69$ N. Now, the deformation of MPAM is re-calculated with $F = F^* = 1.69$ N force where the deflection is 6.9 mm for 45 mm MPAM. The procedure is repeated as shown in Table 1. The value of deformation of MPAM to achieve equilibrium is found out to be 6.9 mm. The pose of end-effector obtained with final length of MPAM as $45 - 6.9 = 38.1$ mm is shown in Fig. 17 alongside the actual deflection of end-effector. The measured pose of the end-effector matches with the theoretical model with a maximum error of 1 mm at the tip. The time required to solve the forward kinematics is about 0.6 seconds on an Intel Pentium PC at 2.0 GHz.

Fig. 18 shows the comparison between theoretical and measured pose for MPAM-*G* actuated at 551.6 kPa (80 psi). The maximum error in tip deflection in this case is also found to be about 1 mm.

Table 1: R at $P_i = 689.4$ kPa

F (N)	Δ (mm)	δ_e (mm)	F^* (N)
0	7.6	22.8	1.69
1.69	6.9	20.4	1.51
1.51	6.9	20.4	1.51

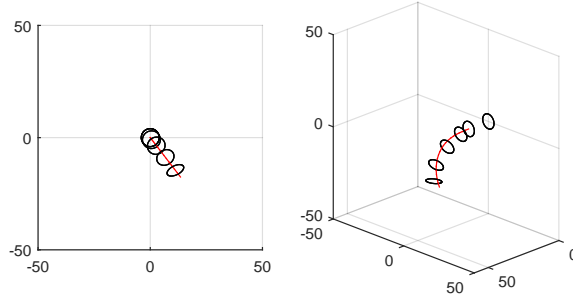


Figure 17: MPAM R actuated at 689.4 kPa

The following steps summarize the method in finding the final pose of end-effector when two MPAMs (say R and G) are actuated:

1. Pose of end-effector ξ_1 when MPAM-R is pressurized individually is found out using the above formulation; tip deflection vector \mathbf{d}_1 is calculated. Likewise ξ_2 is found out when MPAM-G is pressurized individually and corresponding \mathbf{d}_2 is calculated.
2. Angle of end-point vector of MPAM-R is calculated using the equation:

$$\beta_1 = \cos^{-1} \left(\frac{\mathbf{x}_b^n - \mathbf{x}_b^{n-1}}{\|\mathbf{x}_b^n - \mathbf{x}_b^{n-1}\|} \cdot \hat{\mathbf{k}} \right) \quad (29)$$

3. Axis vector $\hat{\mathbf{q}}_1$ is found out using the equation:

$$\hat{\mathbf{q}}_1 = \frac{\mathbf{x}^n - \mathbf{x}^{n-1}}{\|\mathbf{x}^n - \mathbf{x}^{n-1}\|} \times \frac{\mathbf{x}^{n-2} - \mathbf{x}^{n-1}}{\|\mathbf{x}^{n-2} - \mathbf{x}^{n-1}\|} \quad (30)$$

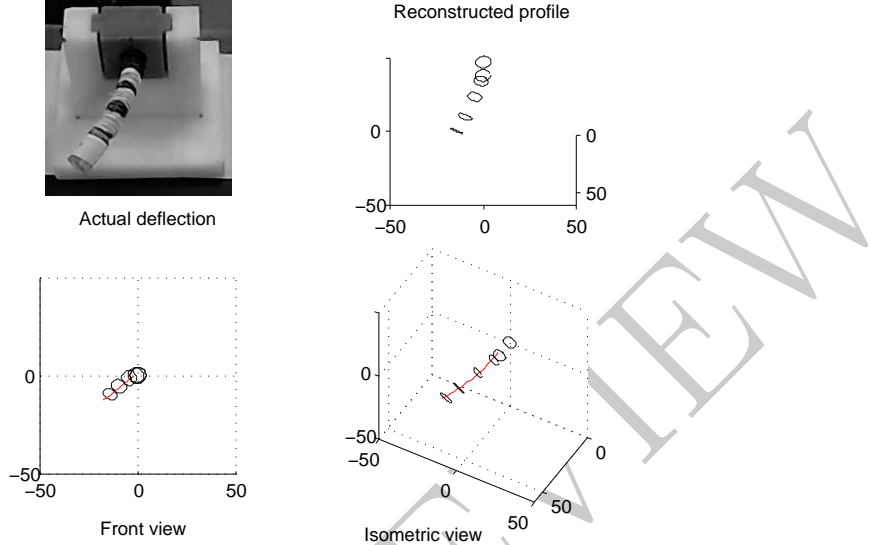


Figure 18: MPAM G actuated at 551.6 kPa

4. Rotation matrix $\hat{\mathbf{R}}_{(\hat{\mathbf{q}}_1, \beta_1)}$ is populated using axis-angle method [37] and tip displacement of second MPAM (MPAM-G), \mathbf{d}_2 is rotated to get \mathbf{d}'_2 .
5. Direction cosines of \mathbf{a}_r are calculated using (28). The plane containing the vector \mathbf{a}_r as well as the $\hat{\mathbf{k}}$ axis can be defined by its normal vector $(m_r)\hat{\mathbf{i}} + (-l_r)\hat{\mathbf{j}}$.
6. A straight line is drawn from the vector $l_0\hat{\mathbf{k}} + \mathbf{d}_1$ in the direction of \mathbf{d}'_2 . The intersection of this line with the plane defined in step 4) gives the final tip position.
7. The iteration is repeated with $n \rightarrow n - 1$ for the entire length of end-effector to obtain the final pose.

Fig. 19 shows the final deformation of end-effector when two MPAMs are actuated by 689.4 kPa (100 psi). The experimental results agree with the theoretical model with approximately 1 mm error at the tip. For example, the deformation and axial force for a 413 kPa (60 psi) pressure input are $\delta_e = 15.8$ mm as well as $F = 1.17$ N respectively. The direction cosines of \mathbf{a}_r calculated using $F_1 = 1.51$ N (corresponding to 689 kPa pressure) and $F_2 = 1.17$ N (corresponding to 413 kPa pressure) are $l_r = -0.17$ and

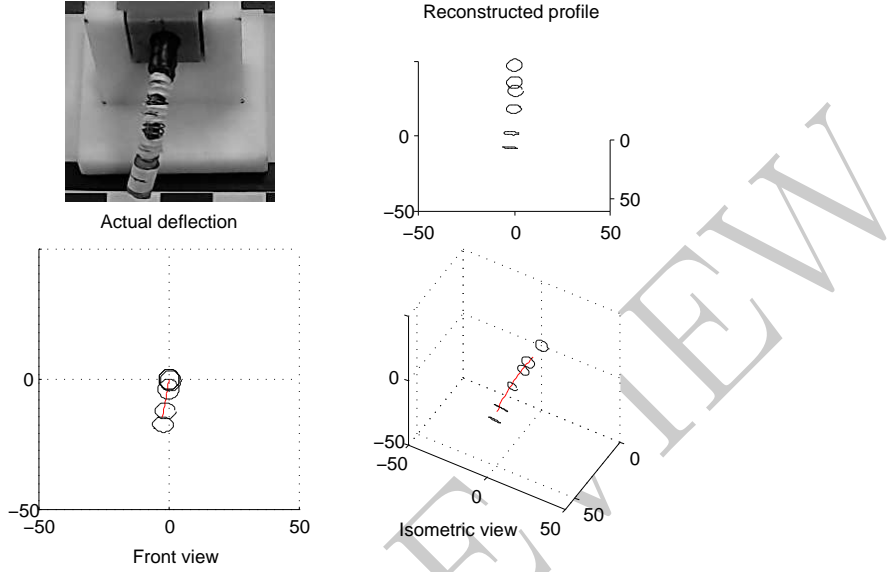


Figure 19: MPAMs R, G actuated at 689.4 kPa

$m_r = -0.7$ respectively—i.e, the plane forms an angle 13.3° with the \hat{j} axis. For a pressure combination of 413 kPa for MPAM- R and 689 kPa for MPAM- G , the results are shown in Fig. 20. The predicted data as well as the reconstructed image for all the results show the promise of employing the developed theoretical formulation in model based control strategies.

Ex-vivo experiments conducted on animal tissue [38] show that the end-effector does not cause perforation even at high value of applied pressure (see accompanying video). This is because unlike cable-driven robots where desired position is attained by directly controlling the cable lengths and a force overload needs to be sensed and controlled. In our case the positioning of the end-effector is achieved indirectly through control of the applied pressure. When a pressure is applied, in the absence of contact with environment, the end-effector will deform as per the statics of the device. If the end-effector is in contact with the environment, the applied pressure will lead to deformation of the end-effector and not the usually stiffer environment. Moreover, the applied force at the tip for maximum pressure is only about 0.2 N which is experimentally verified to be adequate for deflecting all commonly used endoscopic catheters up to 15 mm in all directions (video shows end-effector lifting 10 gms).

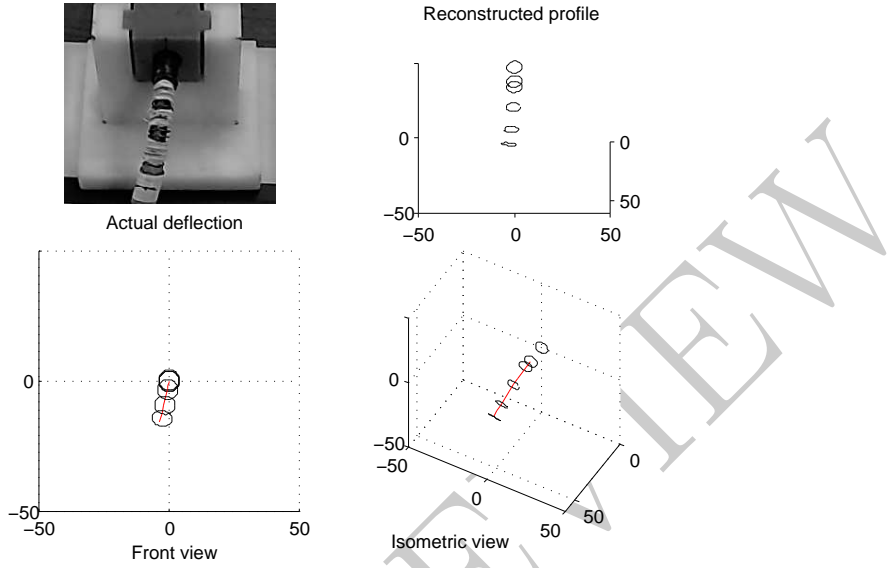


Figure 20: MPAM G at 689.4 kPa and R at 413 kPa

6 Conclusion

This paper deals with the modeling, analysis and experimental validation of a novel independently actuated flexible end-effector. The end-effector is actuated by three miniaturized pneumatic artificial muscles (MPAM). For analysis and control, a new static model of the MPAM is developed based on the static equations of a thick cylinder for the silicone tube and the braiding in the MPAM as a constraint. The novel developed model of the MPAM contains six parameters, including one representing unmodeled effects such as friction and other nonlinearities, and all the six parameters are solved for using mechanics equations. The numerical solutions of the model gives the deformation of the MPAM and this is shown to agree with experimental results with less than 5% error. The improved developed model is also compared with existing models of MPAM and it is shown that the developed model predicts the deformation more accurately.

The end-effector developed does not have guiding discs used in other cable driven system. The kinematics of the actuated end-effector, taking into account the absence of guiding discs, is formulated as a constrained optimization problem. For an applied pressure in one or more MPAMs, first

the change in length is obtained from the developed MPAM model and then the position and orientation of the end-effector is obtained using an iterative scheme. Experiments performed on the developed prototype show that the tip of the end-effector can be positioned in an approximate hemispherical section of 45 mm radius. Using 3D profile reconstruction of the images obtained during experimentation, it is shown that the maximum position error at the tip of the end-effector between the predictions from the forward kinematic model and experiments is 2 ± 1 mm.

At present, the computation time for the forward kinematics is of the order of 0.6 seconds on a desktop PC and this is due to the iterative solution of the constrained optimization problem. Attempts are being made to reduce this time for efficient real-time control. While the developed proof of concept shows that MPAM based end-effector has definite advantages in endoscopic catheter actuation, more work is required before the same can be employed in a clinical setting.

References

- [1] B. P. M. Yeung and T. Gourlay, "A technical review of flexible endoscopic multitasking platforms," *International Journal of Surgery*, vol. 10, no. 7, pp. 345–354, 2012.
- [2] L. Zorn, F. Nageotte, P. Zanne, A. Legner, B. Dallemande, J. Marescaux, and M. de Mathelin, "A novel telemanipulated robotic assistant for surgical endoscopy: Preclinical application to esd," *IEEE Transactions on Biomedical Engineering*, 2017.
- [3] I. A. Gravagne and I. D. Walker, "On the kinematics of remotely-actuated continuum robots," in *Robotics and Automation, 2000. Proceedings. ICRA'00. IEEE International Conference on*, vol. 3. IEEE, 2000, pp. 2544–2550.
- [4] K. Xu, R. E. Goldman, J. Ding, P. K. Allen, D. L. Fowler, and N. Simaan, "System design of an insertable robotic effector platform for single port access (spa) surgery," in *Intelligent Robots and Systems, 2009. IROS 2009. IEEE/RSJ International Conference on*. IEEE, 2009, pp. 5546–5552.

- [5] J. Szewczyk, V. De Sars, P. Bidaud, and G. Dumont, “An active tubular polyarticulated micro-system for flexible endoscope,” *Experimental Robotics VII*, pp. 179–188, 2001.
- [6] V. Kumbhari and M. A. Khashab, “Perforation due to ercp,” *Techniques in Gastrointestinal Endoscopy*, vol. 16, no. 4, pp. 187–194, 2014.
- [7] A. De Greef, P. Lambert, and A. Delchambre, “Towards flexible medical instruments: Review of flexible fluidic actuators,” *Precision Engineering*, vol. 33, no. 4, pp. 311–321, 2009.
- [8] R. H. Gaylord, “Fluid actuated motor system and stroking device,” Jul. 22 1958, US Patent 2,844,126.
- [9] H. Schulte, “The application of external power in prosthetics and orthotics,” *The Characteristics of the McKibben Artificial Muscle, National Research Council*, vol. 874, 1961.
- [10] M. De Volder, A. Moers, and D. Reynaerts, “Fabrication and control of miniature mckibben actuators,” *Sensors and Actuators A: Physical*, vol. 166, no. 1, pp. 111–116, 2011.
- [11] S. Chakravarthy, K. Aditya, and A. Ghosal, “Experimental characterization and control of miniaturized pneumatic artificial muscle,” *Journal of Medical Devices*, vol. 8, no. 4, p. 041011, 2014.
- [12] S. Kurumaya, H. Nabae, G. Endo, and K. Suzumori, “Design of thin mckibben muscle and multifilament structure,” *Sensors and Actuators A: Physical*, vol. 261, pp. 66–74, 2017.
- [13] D. Trivedi, C. D. Rahn, W. M. Kier, and I. D. Walker, “Soft robotics: Biological inspiration, state of the art, and future research,” *Applied bionics and biomechanics*, vol. 5, no. 3, pp. 99–117, 2008.
- [14] K. Xu and N. Simaan, “An investigation of the intrinsic force sensing capabilities of continuum robots,” *IEEE Transactions on Robotics*, vol. 24, no. 3, pp. 576–587, 2008.
- [15] D. Büchler, H. Ott, and J. Peters, “A lightweight robotic arm with pneumatic muscles for robot learning,” in *Robotics and Automation (ICRA), 2016 IEEE International Conference on*. IEEE, 2016, pp. 4086–4092.

- [16] H. Li, K. Kawashima, K. Tadano, S. Ganguly, and S. Nakano, “Achieving haptic perception in forceps manipulator using pneumatic artificial muscle,” *IEEE/ASME Transactions on Mechatronics*, vol. 18, no. 1, pp. 74–85, 2013.
- [17] P. K. Jamwal, S. Q. Xie, S. Hussain, and J. G. Parsons, “An adaptive wearable parallel robot for the treatment of ankle injuries,” *IEEE/ASME Transactions on Mechatronics*, vol. 19, no. 1, pp. 64–75, 2014.
- [18] R. Kang, Y. Guo, L. Chen, D. T. Branson III, and J. S. Dai, “Design of a pneumatic muscle based continuum robot with embedded tendons,” *IEEE/ASME Transactions on Mechatronics*, vol. 22, no. 2, pp. 751–761, 2017.
- [19] G. Andrikopoulos, G. Nikolakopoulos, and S. Manesis, “A survey on applications of pneumatic artificial muscles,” in *Control & Automation (MED), 2011 19th Mediterranean Conference on*. IEEE, 2011, pp. 1439–1446.
- [20] R. M. Robinson, C. S. Kothera, R. M. Sanner, and N. M. Wereley, “Nonlinear control of robotic manipulators driven by pneumatic artificial muscles,” *IEEE/ASME Transactions on Mechatronics*, vol. 21, no. 1, pp. 55–68, 2016.
- [21] B. Tondu, “Modelling of the mckibben artificial muscle: A review,” *Journal of Intelligent Material Systems and Structures*, vol. 23, no. 3, pp. 225–253, 2012.
- [22] D. Chen and K. Ushijima, “Prediction of the mechanical performance of mckibben artificial muscle actuator,” *International Journal of Mechanical Sciences*, vol. 78, pp. 183–192, 2014.
- [23] G. Andrikopoulos, G. Nikolakopoulos, and S. Manesis, “Novel considerations on static force modeling of pneumatic muscle actuators,” *IEEE/ASME Transactions on Mechatronics*, vol. 21, no. 6, pp. 2647–2659, 2016.
- [24] W. Liu and C. Rahn, “Fiber-reinforced membrane models of mckibben actuators,” *Transactions of the ASME-E-Journal of Applied Mechanics*, vol. 70, no. 6, pp. 853–859, 2003.

- [25] C. S. Kothera, M. Jangid, J. Sirohi, and N. M. Wereley, “Experimental characterization and static modeling of mckibben actuators,” *Journal of Mechanical Design*, vol. 131, no. 9, p. 091010, 2009.
- [26] K. Ashwin, D. P. Jose, and A. Ghosal, “Modeling and analysis of a flexible end-effector for actuating endoscopic catheters,” in *Proceedings of the 14th IFToMM World Congress*. IFToMM, 2015, pp. 113–120.
- [27] MATLAB, “7.12. 0.635 (r2011a) The MathWorks Inc.” Natick, Massachusetts, United States, 2011.
- [28] C. S. Jog, *Continuum Mechanics*. Cambridge University Press, 2015, vol. 1.
- [29] C.-P. Chou and B. Hannaford, “Measurement and modeling of mckibben pneumatic artificial muscles,” *IEEE Transactions on Robotics and Automation*, vol. 12, no. 1, pp. 90–102, 1996.
- [30] S. Davis and D. G. Caldwell, “Braid effects on contractile range and friction modeling in pneumatic muscle actuators,” *The International Journal of Robotics Research*, vol. 25, no. 4, pp. 359–369, 2006.
- [31] D. G. Caldwell, N. Tsagarakis, and G. Medrano-Cerda, “Bio-mimetic actuators: polymeric pseudo muscular actuators and pneumatic muscle actuators for biological emulation,” *Mechatronics*, vol. 10, no. 4, pp. 499–530, 2000.
- [32] N. Simaan, R. Taylor, and P. Flint, “A dexterous system for laryngeal surgery,” in *Robotics and Automation, 2004. Proceedings. ICRA ’04. 2004 IEEE International Conference on*, vol. 1. IEEE, 2004, pp. 351–357.
- [33] D. B. Camarillo, C. F. Milne, C. R. Carlson, M. R. Zinn, and J. K. Salisbury, “Mechanics modeling of tendon-driven continuum manipulators,” *IEEE Transactions on Robotics*, vol. 24, no. 6, pp. 1262–1273, 2008.
- [34] T. Kato, I. Okumura, S.-E. Song, A. J. Golby, and N. Hata, “Tendon-driven continuum robot for endoscopic surgery: Preclinical development and validation of a tension propagation model,” *IEEE/ASME Transactions on Mechatronics*, vol. 20, no. 5, pp. 2252–2263, 2015.

- [35] M. S. Menon, G. Ananthasuresh, and A. Ghosal, “Natural motion of one-dimensional flexible objects using minimization approaches,” *Mechanism and Machine Theory*, vol. 67, pp. 64–76, 2013.
- [36] R. Hartley and A. Zisserman, *Multiple View Geometry in Computer Vision*. Cambridge University Press, 2003.
- [37] A. Ghosal, *Robotics: Fundamental Concepts and Analysis*. Oxford University Press, 2006.
- [38] E. L. Artifon, S. Cheng, T. T. Nakadomari, L. Kashiwagi, J. C. Ardengh, E. Belmonte, and J. P. Otoch, “Ex vivos models to teaching therapeutic endoscopic ultrasound (t-eus),” *Revista de Gastroenterología del Perú*, vol. 38, no. 1, pp. 103–110, 2018.